

Investigation of neutron scattering in the Multi-Blade detector with Geant4 simulations

G. Galgóczi^{a,b} K. Kanaki^{c,1} F. Piscitelli^c T. Kittelmann^c D. Varga^b R. Hall-Wilton^{c,d}

^a*Eötvös Loránd University, 1053 Budapest, Egyetem tér 1-3., Hungary*

^b*Hungarian Academy of Sciences, Wigner Research Centre for Physics, 1525 Budapest 114., Hungary*

^c*European Spallation Source ESS ERIC, SE-221 00 Lund, Sweden*

^d*Mid-Sweden University, SE-851 70 Sundsvall, Sweden*

E-mail: Kalliopi.Kanaki@esss.se

ABSTRACT: The European Spallation Source (ESS) is the world's next generation spallation-based neutron source. The research conducted at ESS will yield in the discovery and development of new materials including the fields of manufacturing, pharmaceuticals, aerospace, engines, plastics, energy, telecommunications, transportation, information technology and biotechnology. The spallation source will deliver an unprecedented neutron flux. In particular, the reflectometers selected for construction, ESTIA and FREIA, have to fulfill challenging requirements. Local incident peak rate can reach 10^5 Hz/mm². For new science to be addressed, the spatial resolution is aimed to be less than 1 mm with a desired scattering of 10^{-4} (peak-to-tail ratio). The latter requirement is approximately two orders of magnitude better than the current state-of-the-art detectors. The main aim of this work is to quantify the cumulative contribution of various detector components to the scattering of neutrons and to prove that the respective effect is within the requirements set for the Multi-Blade detector by the ESS reflectometers. To this end, different sets of geometry and beam parameters are investigated, with primary focus on the cathode coating and the detector window thickness.

KEYWORDS: Boron-10, Geant4 simulations, neutron scattering, thermal neutron detection

¹Corresponding author.

Contents

1	Introduction	1
2	The Multi-Blade model in Geant4	2
2.1	The Multi-Blade detector	2
2.2	Implementation of the detector model in Geant4	3
2.3	Implementation of the detection process in the simulation	4
2.4	Comparison of detection efficiency obtained by measurements and Geant4	4
3	Scattering effects	5
3.1	Definition of spurious detection events	5
3.2	Comparison of simulation with experimental results	8
3.3	Impact of the converter thickness	9
3.4	Impact of the detector window thickness	10
4	Conclusions	12
A	NCrystal cross sections	16

1 Introduction

The ESS ERIC [1], currently under construction in Lund, Sweden, aspires to become the most powerful pulsed neutron source in the world. With its long pulse of 2.86 ms and a brilliance higher than 10^{14} n/cm²/s/sr/Å, it can deliver unprecedented flux on the sample and revolutionise the way neutron experiments are conducted [2, 3]. The produced neutrons are destined to serve a variety of instruments for reflectometry, diffraction, spectrometry and imaging purposes. According to the current schedule the first neutrons will hit the target in 2019, with the user programme starting in 2023.

Reflectometry is an experimental technique present at every neutron source. Hence, two of the first instruments approved for construction at ESS are reflectometers. The one, with a vertical scattering plane, is called the Fast Reflectometer for Extended Interfacial Analysis (FREIA) [4–6] and the horizontal one is ESTIA [7–9]. The former one will be optimised for magnetic samples and in-situ or in-operando studies. The latter reflectometer is designed to achieve the best performance for liquid/liquid or liquid/gas interfaces. With a sample flux of 10^9 - 10^{10} n/s/cm² and a high sample reflectivity ($\sim 90\%$) it is expected that the peak instantaneous rate of the neutron detectors could reach 100 kHz/mm² [7–9]. This value exceeds the rate capability of current neutron detector technologies (including ³He-based detectors) by approximately two orders of magnitude. Additionally, the limit set for neutron scattering inside the detector is lower than what the current state-of-the-art

detectors are capable of [10]. These are the two biggest challenges for the detector design aimed at reflectometry for ESS.

In the past ^3He -based neutron detectors played a key role for thermal and cold neutron detection [11]. Due to the limitations of these detectors in scientific performance and the shortage of ^3He [12, 13], the focus of the neutron detector community has shifted to alternative, higher-performing solutions, such as $^{10}\text{B}_4\text{C}$ -based detectors [14–20], scintillators [21–28] or ^6LiF -based solid state silicon detectors [29–31]. Additionally, it is already proven that $^{10}\text{B}_4\text{C}$ -based detectors are capable of outperforming ^3He detectors in terms of spurious scattering of neutrons [10, 32]. Several studies demonstrate the performance of this detector type and its suitability for neutron scattering experiments [32–35].

The detector design developed and adopted for the ESS reflectometers is the Multi-Blade detector [32–37]. It has been extensively characterised and validated at various neutron facilities and with various types of samples. To get a deeper understanding of the scattering patterns the detector geometry causes and to support the choice of materials and component dimensions, a detailed Geant4 [38–40] detector model is implemented. The main aim of this simulation effort is to prove that the Multi-Blade detector meets the requirements set by ESS, particularly the scattering of 10^{-4} (see p.9, figure 9.1 in [8]).

In the following sections the Multi-Blade detector is introduced. The details of the Geant4 implementation are presented, as well as the figure of merit used in the subsequent analysis. Fractional scattering is defined and sources of background caused by misplaced detection events are identified and studied as a function of neutron wavelength. The results are discussed with respect to the instrument requirements.

2 The Multi-Blade model in Geant4

2.1 The Multi-Blade detector

The Multi-Blade detector is a novel neutron detector currently being designed at ESS (see figure 1a). Its development was initiated at Institute Laue-Langevin (ILL) [35, 37, 41, 42]. It consists of a set of successive Multi-Wire Proportional Chambers [43], with $^{10}\text{B}_4\text{C}$ -coated cathodes and Ar/ CO_2 (80/20 by volume) as a gas counter mixture. In addition to the anode wires, each chamber is equipped with a strip readout. The strips are perpendicular to the wire direction, in order to achieve two-dimensional spatial resolution.

The detector consists of cassettes as building units. Each one has a boron carbide ($^{10}\text{B}_4\text{C}$) converter layer that is on a titanium substrate called a “blade”. On the other side of the blade a kapton layer and 32 copper strips are located for charge readout. Between the blades 32 wires are stretched at a 4 mm pitch. The blades are tilted in a way that the incoming neutron beam hits the converter layer with an incident angle of 5° , as shown in figure 1b. Therefore the thickness of the converter is viewed by the neutrons as being effectively about 11 times larger [32, 44]. Several cassettes are assembled together forming a fan-like arrangement to achieve the area coverage required for reflectometry.

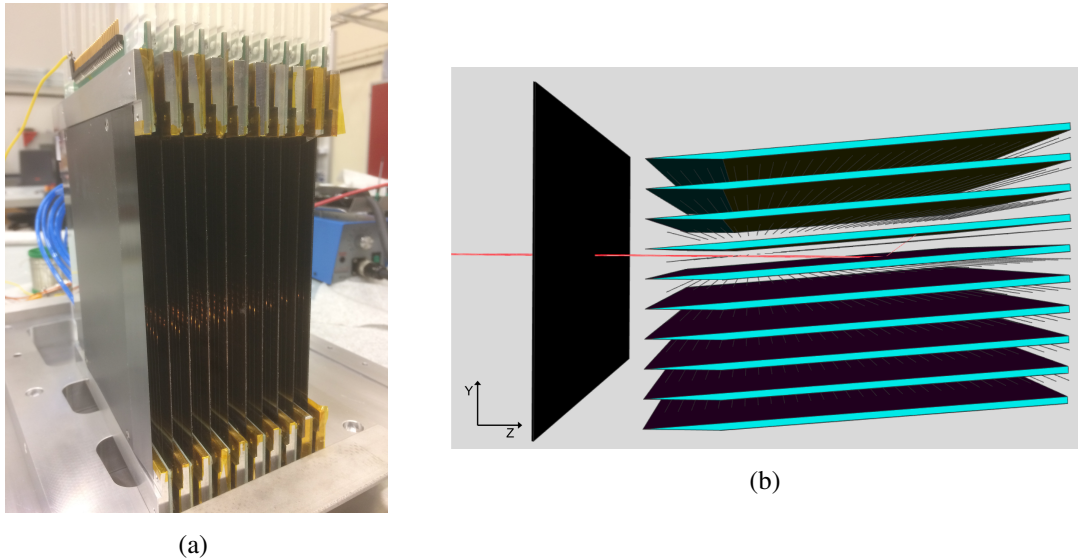


Figure 1: (a) A prototype of the Multi-Blade detector [33]. (b) Geant4 geometry model being hit by a red neutron beam through the detector entrance window. The vessel is absent from both figures to allow a clear view of the geometry.

2.2 Implementation of the detector model in Geant4

It is exactly this fan-like geometry that is the core of the current simulation study. The detector geometry and data analysis are implemented in a framework based on Geant4 developed by the ESS Detector Group [45, 46]. The detector geometry consists of ten $130 \text{ mm} \times 140 \text{ mm} \times 2 \text{ mm}$ titanium blades coated with enriched $^{10}\text{B}_4\text{C}$ by 98% on one side and a kapton and copper layer on the other, with thicknesses of $30 \mu\text{m}$ and $40 \mu\text{m}$ respectively. The copper layer is not segmented in strips, unlike the real prototype, as the distance between the strips is 0.1-0.2 mm and the effect of spurious scattering in this part of the detector is negligible compared to other materials. The tungsten wires are also included in the model. The Ar/CO₂ mixture has a ratio of 80/20 by volume and a pressure of 1.1 bar. The gas vessel surrounds the entire detector structure. It consists of enriched $^{10}\text{B}_4\text{C}$ acting as a total absorber, in order to prevent scattered neutrons from entering the active volume again. On the beam entrance side an aluminium window allows the neutrons to reach the converter (see figure 1b).

All materials are selected from the Geant4 database of NIST materials, except for Ti, Al, Cu and W. The latter are described with the use of the NCrystal library [46, 47], as their crystalline structure is important for the correct treatment of their interaction with thermal neutrons. The physics list used is QGSP_BIC_HP and the Geant4 version is 10.00.p03.

Last, but not least, the neutron generator is a mono-energetic pencil beam, impinging the converter layer at a 5° angle in the centre of the middle blade, as in figure 1b. The generator parameters, albeit simple, condense the characteristics of typical neutron distributions from reflectometry samples that are important for this study. All results are produced with 1 million events.

2.3 Implementation of the detection process in the simulation

In boron-based neutron detectors the secondary charged particles (α and ${}^7\text{Li}$ ions) are created after the ${}^{10}\text{B}$ nucleus captures a neutron. The cross section of this process is 3835 b for neutrons with a wavelength of 1.8 Å (p. 15, [11]). The position where the neutron is absorbed is called the conversion point. Therefore the neutrons are detected indirectly. The ion products cross the converter and enter the gas volume with a remaining energy. The maximum distance the ${}^7\text{Li}$ and α ions can travel in the specific counting gas is 3 mm and 6 mm respectively at atmospheric pressure and room temperature conditions.

In order to describe the physical phenomena behind the detection of neutrons in the Multi-Blade detector, an approximation is used. The geometrical center of the tracks of the charged particles created by ionisation in the gas of the detector is defined as the hit position (see figure 2). Furthermore, the fact that the readout of the hits is done by wires and strips has to be taken into account. For example, in the direction perpendicular to the blades surface, the coordinate of the hit is measured by the wires. Therefore the position of the triggered wire is read out, not the actual position of the centre of the charge cloud. In order to emulate this effect, the hits are projected to the plane of the boron surface, a transformation that brings the simulation treatment closer to the experimental process.

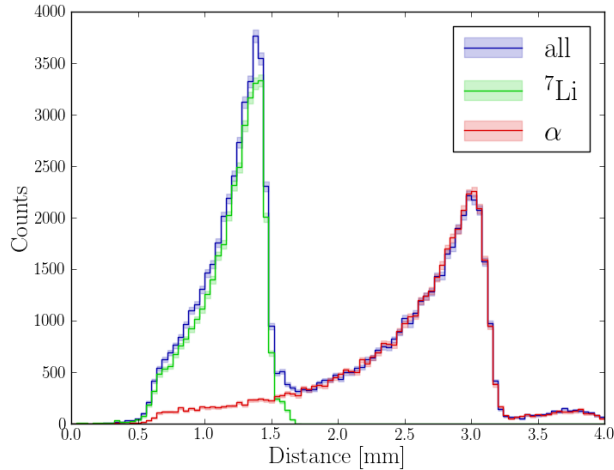


Figure 2: Distance between conversion and hit position as approximated in a simulation for 12 Å neutrons. The two peaks reflect the maximum path of ${}^7\text{Li}$ and α ions respectively, but are halved in this representation (1.5 mm and 3 mm) as a result of the hit definition. The bands around the lines represent the statistical uncertainties.

2.4 Comparison of detection efficiency obtained by measurements and Geant4

The simulation results produced with the ESS simulation framework have been previously validated in [48]. An additional validation of the current model is performed in terms of detection efficiency. The results are compared to analytical calculations [37] and experimental measurements performed at the ATHOS instrument of the BNC facility [32] in Hungary and CRISP [33, 36] at ISIS, UK. The observed agreement is within the error bars for most of the neutron wavelengths. The uncertainties of the experimental points depend on the statistics of each measurement and systematic effects on

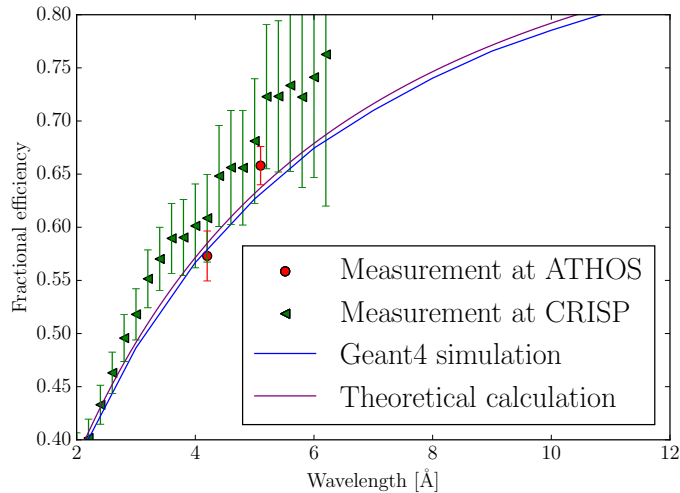


Figure 3: Fractional detection efficiency of the Multi-Blade detector as a function of neutron wavelength, obtained from theoretical calculations [37, 49], measurements [32, 33] and Geant4 simulation (this work).

the experimental data are not accounted for in the simulation. In addition, the efficiency estimate of the simulation is affected to a small extent by the fact that the detector gas volume is not segmented in the simulation. The detection threshold of 120 keV on the energy deposition is applied per event for the entire gas volume and not per wire, as in the experimental data. However, due to the localised nature of the energy deposition the approximation does not compromise the simulation for the purposes of this work.

3 Scattering effects

3.1 Definition of spurious detection events

The Multi-Blade is a position sensitive detector, intended to operate in Time-of-Flight (TOF) mode. This means that the energy of the incident neutron is indirectly derived from a time and a 3D position measurement. Two factors can impact the precision of the neutron position reconstruction; the detector spatial resolution (short-scale effect) and scattering (long-scale effect), with different impact to the distribution of the detection coordinates. Figure 4 demonstrates these scenarios. In figure 4a a neutron, which is absorbed in the first converter layer it meets, leads to a secondary particle releasing its energy in the counting gas (the other particle gets stopped inside the cathode substrate and is therefore lost). The spatial resolution of the detector determined by the anode wire pitch and the strip width locally smears the experimental detection point in the data reconstruction process. Figures 4b and 4c depict long-range effects stemming from neutron scattering either within the detector itself or in the entrance window respectively. Such events lead to the miscalculation of the distance between sample and detection point, and eventually to a wrongly derived value for the incident neutron energy and scattering vector.

In order to quantify the impact of the misplaced detected neutrons, a nonphysical technical Geant4 particle, called “geantino”, is utilised. This particle is generated along with each primary neutron with the same initial parameters (see figure 4c). Geantinos do not interact with matter,

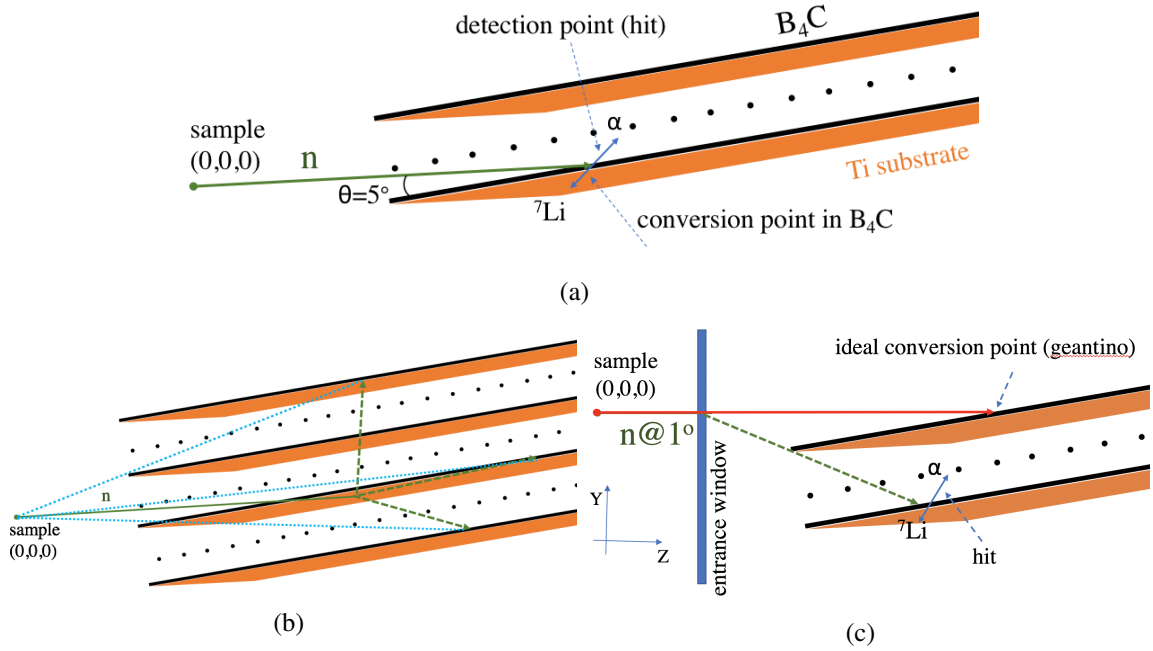


Figure 4: (a) Difference between conversion and detection point. (b) A neutron traversing the first converter layer (solid green) can scatter in the blade material and finally get converted away from the first crossing point (dashed green). This leads to the miscalculation of the distance between sample and detection point (dashed blue). (c) Similarly for a scattered neutron on the detector window. The latter is 1° inclined with respect to the vertical axis. The projection of the detection point on the converter layer is not displayed here for view simplification.

therefore their tracks are straight lines. The point where a primary neutron would be detected in an ideal measurement is defined by the intersection of the respective geantino track with the first converter layer it traverses. This position is then compared against the respective neutron detection coordinates. The definition of this condition is motivated by the detector design; the actual thickness of the converter is at least $7.5 \mu\text{m}$ [32, 33] to ensure that, aside from a high detection efficiency, almost all neutrons convert in the first boron layer they encounter, thus reducing the scattering caused by the cathode material.

The utilisation of geantinos allows for this study to be realised for arbitrary generators and geometries. However, in the current one, due to the fact that primary neutrons start from $(0,0,0)$ and form a pencil beam on the Z axis, the geantino “detection” coordinates are also 0 in X and Y. This means that the actual neutron hit coordinates are sufficient for the visualisation of scattering effects in this particular case ($X_{\text{hit}} - X_{\text{geantino}} = X_{\text{hit}}$, $Y_{\text{hit}} - Y_{\text{geantino}} = Y_{\text{hit}}$). These hit coordinates are the ones projected on the converter layer as explained at the end of subsection 2.3.

The contributors to the scattering effects studied in this work are the converter layer and the entrance window of the detector, both looked at as a function of neutron wavelength. The material (Ti) and thickness of the blade (2 mm) have been dictated by engineering needs and the coating process and are fixed for all simulations of this work.

A visualisation of the scattered hits projected on the detector window appear in figure 5. The projection is necessary as the window is not vertical but has a 1° angle with respect to the Y-axis.

It is also the standard way of experimentally visualising the data

The primary neutrons hit the centre of the distribution in figure 5a. The simulation is run for the extreme case of 1 Å for the neutron wavelength and 1 cm for the window thickness, in order to maximise the scattering effects. The entries away from the centre make up the scattering events. The asymmetry of the distribution reflects the asymmetry in the registration of the detection events due to the orientation of the blades with respect to the incident beam. The latter effect is better demonstrable in the projection of figure 5c. Both figures 5b and 5c depict the short-scale effect attributed to the detector resolution, manifesting itself as the Gaussian smearing around 0. The extended tails on either side of the distribution represent the long-scale scattering events. In the case of figure 5c the tails are “modulated” by the succession of the blades in the Y-direction, in addition to the window effects. Such structures are absent in the X-direction because of the detector symmetry along the wire length.

A detected neutron is considered misplaced, if the detection occurs outside the 4σ ($\sim 2 \times \text{FWHM}$) of the Gaussian fit of the spatial hit distributions (see figures 5b and 5c), i.e. 3.87 mm in the direction parallel to the wires (X-direction) and 0.267 mm in the Y-direction. The σ_X and σ_Y of the two fits indicate minimal impact of scattering on resolution (e.g. $\text{FWHM}_Y^{\text{detector}} = 0.55$ mm and $\text{FWHM}_Y^{\text{fit}} \approx 0.3 \times \text{FWHM}_Y^{\text{detector}}$). The fraction of scattered neutrons is estimated by summing up all hits that fulfil the above condition and dividing this sum with the total number of detected neutrons, as in the equation below

$$Fraction = \frac{N_{\text{scattered neutrons}}(|x| \geq 3.87 \text{ mm and } |y| \geq 0.267 \text{ mm})}{N_{\text{all neutrons}}}_{\text{detected}}. \quad (3.1)$$

This is the figure of merit used in the following subsections, in contrast to the instrument approach, which evaluates the peak-to-tail ratio. The current approach yields higher values of fractional scattering but is important for the detector evaluation.

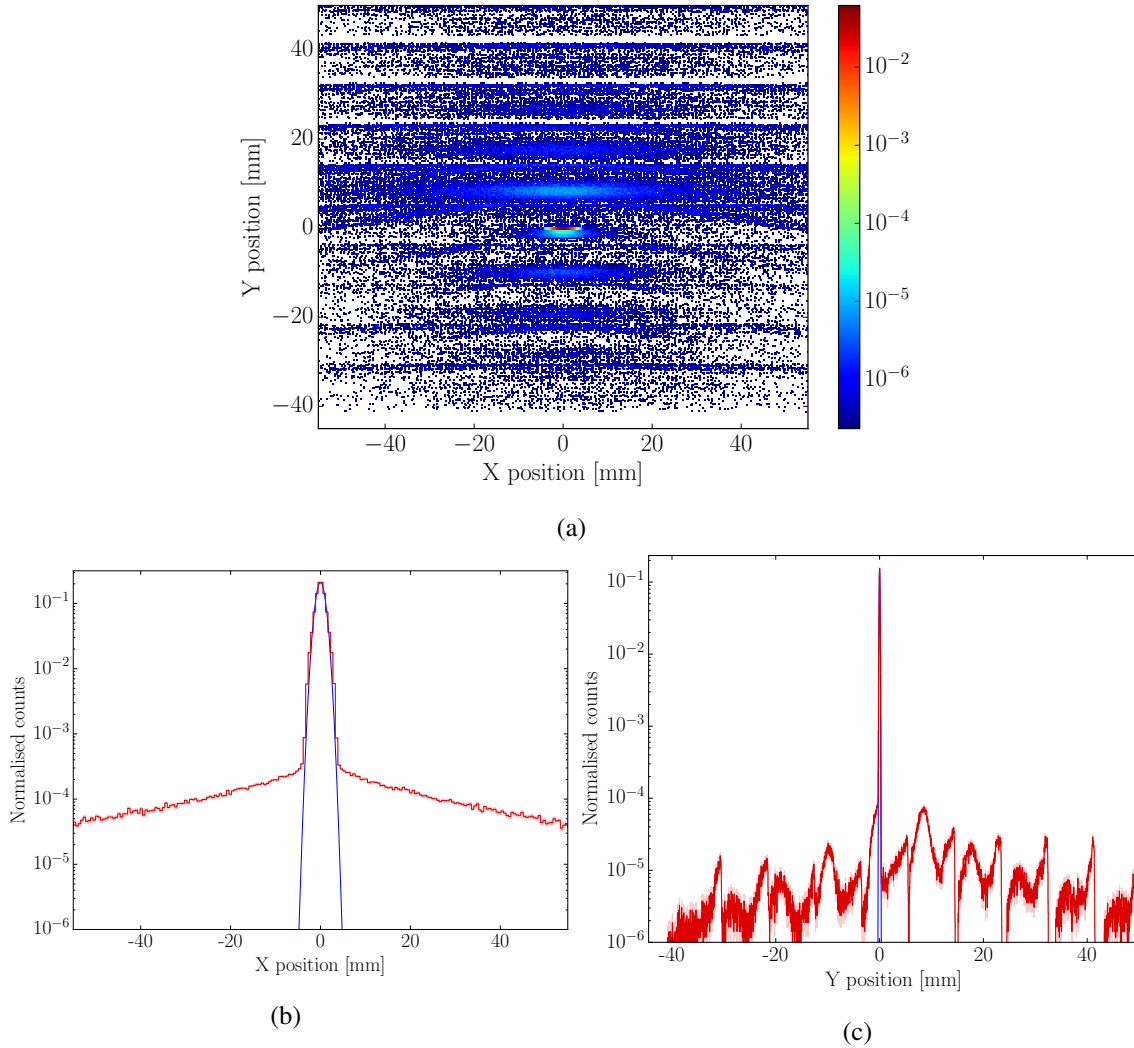


Figure 5: (a) Two-dimensional distribution of hit coordinates, projected on the detector window surface. X (b) and Y (c) projections of distribution (a) in red. The figures are produced with 1 \AA neutron wavelength and a window thickness of 1 cm. All distributions are normalised to 1. A Gauss fit of the central bins (in blue) gives $\sigma_X=0.968 \text{ mm}$ ($\text{FWHM}_X^{fit}=2.27 \text{ mm}$) and $\sigma_Y=0.0667 \text{ mm}$ ($\text{FWHM}_Y^{fit}=0.157 \text{ mm}$).

3.2 Comparison of simulation with experimental results

Recently acquired experimental data allow for a comparison with the simulation results. The measurements [33, 36] were performed at the CRISP neutron reflectometer at the ISIS neutron and muon source [50]. The Geant4 model matches the geometrical choices of the respective demonstrator, i.e. the window thickness is 2 mm and the converter layer is $4.4 \mu\text{m}$ thick in this particular demonstrator. The neutron wavelength in the simulation is set to 1 \AA and the beam is pencil-like, while the experimental beam profile was approximately $3 \text{ mm} \times 60 \text{ mm}$. The simulation simplification serves the purpose of providing a clearer picture of the scattering topology and is justified by the detector symmetry along the X-axis.

The basis of the comparison is the Y position of the detection events, as in figure 5c and is

shown in figure 6. The experimental data correspond to a wavelength range of 0.5-2.5 Å, achieved via the application of a TOF slice (red distribution of figure 10 in [33]). The simulated coordinates are smeared with a Gaussian of $\sigma=0.42$ mm (ca. $2\times$ FWHM) [33, 36]. Only six cassettes were experimentally read-out, therefore only six “peaks” appear in the blue distribution of figure 6. In addition, three wires from the end of each cassette do not contribute to the measurement and have also been accounted for in the simulation by excluding the respective Y histogram bins. The distributions are normalised to their integral.

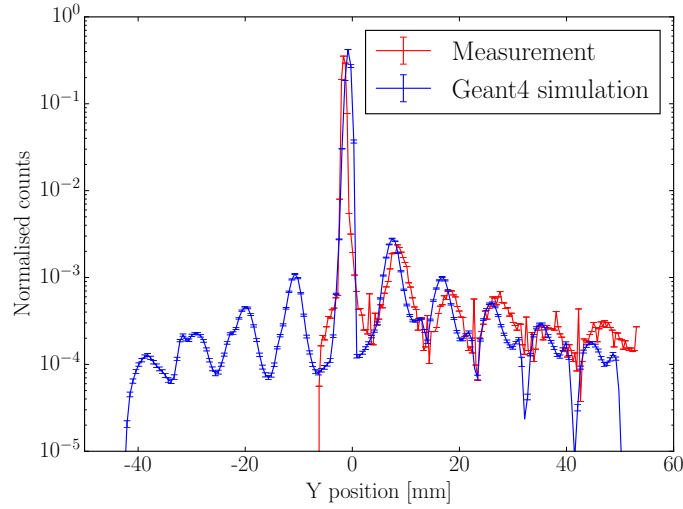


Figure 6: Comparison of Y-position of detected neutrons in measurements taken at CRISP [33] and the results of the simulation (this work).

The Geant4 simulation is able of reproducing the shapes, widths and features of the experimental data. The systematic effects are out of scope of the current work. The shape agreement indicates that the simulation reproduces the location of the scattered events and gives confidence that the topology of scattering is understood in a manner sufficient for the purposes of this study. The fraction of scattered neutrons in the simulation is 3.5%. The same fraction estimated from the experimental data amounts to 3.1%.

3.3 Impact of the converter thickness

In [32, 33] it is argued that an increase of the converter thickness can respectively increase the fraction of absorbed neutrons, if set to a value higher than $4.4 \mu\text{m}$ (figure 11 of [33]). The motivation is to prevent as many neutrons from reaching the titanium blade behind the coating, which is the primary contributor to scattering. The detection efficiency anyway saturates at thicknesses above $3 \mu\text{m}$ [32]. At the same time, an upper value limit needs to be determined, as it is not cost-effective, nor good thin-film deposition practice, to arbitrarily increase the boron carbide thickness.

For the study of the converter thickness the material of the detector window is set to vacuum. Various thicknesses are selected, ranging from typical to extreme. The results are summarised in table 1 and figure 7a, listing the figure of merit defined with equation 3.1.

The table and figure values represent the scattering which is intrinsic to the detector and is primarily attributed to the blade material. Minor contributions come from the counting gas, the

Table 1: Fraction of scattered neutrons in %, as defined in equation 3.1, for various converter thicknesses and neutron wavelengths.

λ [Å]	c. thickness [μm]	0.1	1	5	7.5	10	20
1		22.250	17.310	4.310	1.840	0.831	0.074
2.5		8.570	5.080	0.265	0.067	0.034	0.022
12		0.460	0.098	0.045	0.040	0.038	0.037

converter and the wires. Figure 7b depicts the distribution of the hit Y position for various converter thicknesses. Clearly, the thicker the coating, the higher the probability is that all neutrons convert

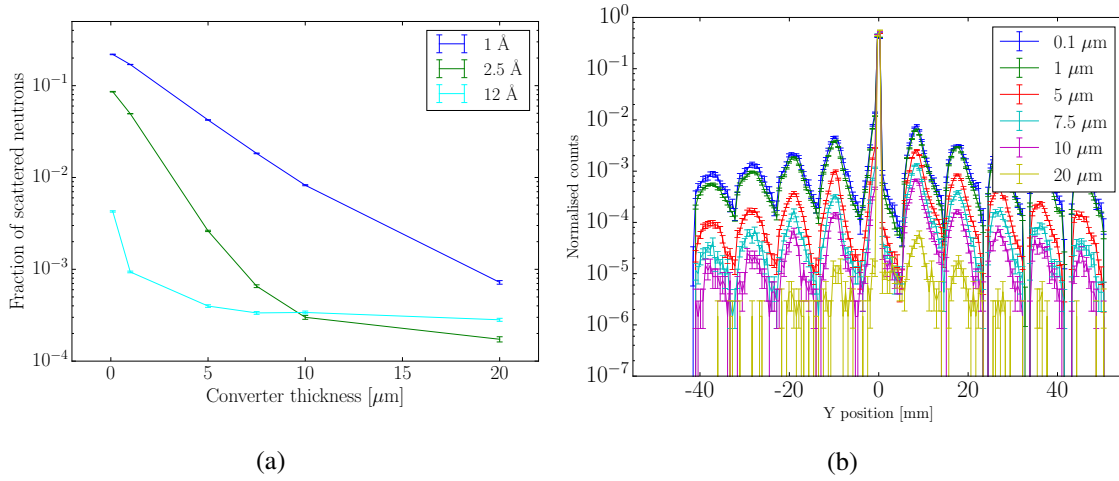


Figure 7: (a) Fraction of scattered neutrons as defined in equation 3.1 as a function of converter thickness for various neutron wavelengths. (b) Y position of hits for various converter thicknesses for a neutron wavelength of 1 Å. The entrance window material is set to vacuum.

and stop in the first layer - regardless of being detected, thus minimising scattering effects inside the detector. Adopting a thickness between 5 μm and 10 μm can reduce the fractional scattering by 1-2 orders of magnitude. The trend in figure 7a demonstrates that for wavelengths above 2.5 Å and 4 Å which are the lowest limit for FREIA and ESTIA respectively, a cost-effective choice of converter thickness would be of the order of 7-8 μm , for the fraction of scattered neutrons to stay below 10^{-3} .

3.4 Impact of the detector window thickness

Following the same methodology, the next parameter to be studied is the thickness of the Al detector window. This item is an integral component of the detector, separates the counting gas from the detector environment and assures its operation in vacuum or atmospheric conditions. Similar studies have been performed with other detector types [48]. The values selected represent typical thicknesses used in neutron instruments, in addition to extreme values. The converter thickness for this series of simulations is now fixed at 7.5 μm . The results are summarised in table 2 and figures 8 and 9. Looking at figure 8, the scattering effects become more significant for lower

neutron wavelengths. The result is consistent with the trend of the scattering (see appendix A), in combination with the absorption cross sections of the materials involved for the specific geometry.

It is interesting to note that a different, e.g. larger detector geometry, would not only scatter differently but also register these events differently. Especially for wavelengths below the Bragg cut-off value of Al and Ti (see figure 10), it is possible to imagine a scenario where the Al window scatters in such a way that although the fraction of scattered neutrons is higher, the scattering angles are such that the neutrons are diverted away from the detector active volume. That is why it is essential to study the impact of the window in combination with the detector response. Scattering is only an issue if it is detected.

The Multi-Blade detector is intended to operate both in vacuum and a normal pressure atmosphere. Given the engineering considerations based on these atmospheric conditions and the fact that the final detector installed at the ESS reflectometers will have a window with a size of 500 mm \times 250 mm, engineering studies show that the window thickness can safely remain below 5 mm for vacuum operation. Recent developments in the ESTIA design promote a neutron flight vessel of a 1 bar Ar/⁴He mixture, in which case the Multi-Blade detector can be operated with a thin foil (ca. 25-100 μ m) instead of a window. In summary, for the wavelengths of interest, the fraction of scattered neutrons at the presence of the window is within acceptable limits.

Table 2: Fraction of scattered neutrons in %, as defined in equation 3.1, as a function of window thickness and neutron wavelength for a converter thickness of 7.5 μ m.

λ [Å]	0	0.1	1	5	10
1	1.840	1.870	1.970	2.480	3.060
2.5	0.063	0.069	0.098	0.238	0.398
4	0.030	0.030	0.039	0.088	0.187
6	0.030	0.031	0.036	0.054	0.075
12	0.041	0.041	0.046	0.073	0.103

The impact of the detector window is also demonstrable in figure 9. In figure 9a the lower peaks on either side of the centre are at least 4 orders of magnitude below the peak containing the non-scattered events, especially for the values of interest above 2.5 Å. This value satisfies the instrument requirement, the way it is defined as a peak-to-tail ratio. As expected, the fractional scattering decreases as neutrons get colder.

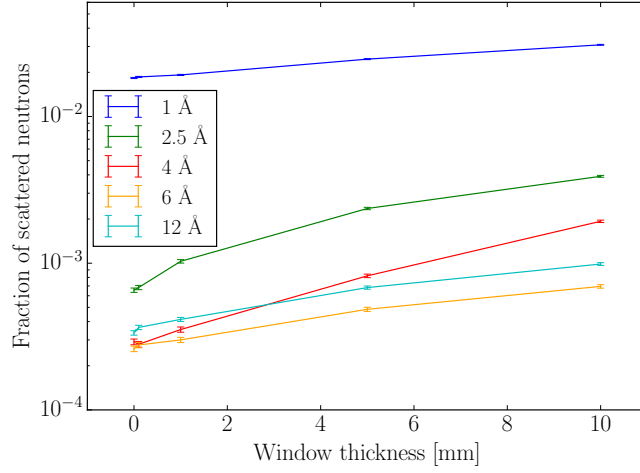


Figure 8: Fraction of scattered neutrons as defined in equation 3.1 as a function of window thickness for various wavelengths and a converter thickness of $7.5 \mu\text{m}$.

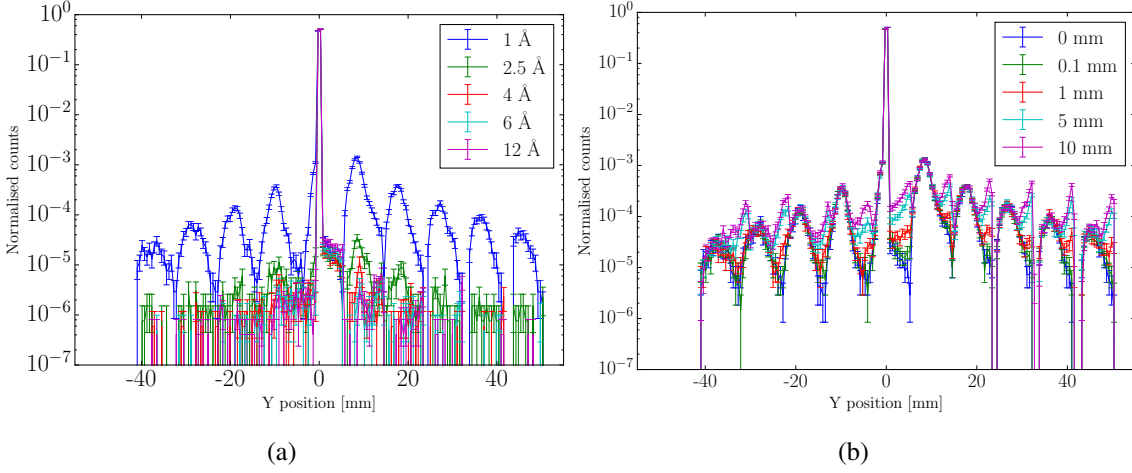


Figure 9: (a) Y position of hits for various neutron wavelengths and no detector window for converter thickness of $7.5 \mu\text{m}$. (b) Same distribution for 1 \AA with varying window thicknesses.

4 Conclusions

A detailed Geant4 model of the Multi-Blade detector is implemented, in order to identify and quantify scattering effects. To this end, a parameter scan is performed focusing mainly on the effects related to the converter thickness and the detector window. The substrate material and thickness have been experimentally optimised and therefore the engineering values are used in the simulation. Various neutron wavelengths of relevance for ESS reflectometry are used.

A comparison of the simulation with experimental results obtained at the CRISP reflectometer confirms our understanding of the detection and scattering topology within the detector. It is shown that the degradation in spatial resolution due to scattering is smaller than the detector resolution. The result of the converter thickness study supports the design choice to increase this value to $7.5 \mu\text{m}$,

with a 2 orders of magnitude gain in terms of scattering suppression. As for the detector window, its impact is within the instrument requirements for the values that result from the engineering studies, in particular for detector operation in vacuum.

Last but not least, this study selects the amount of fractional scattering as a figure of merit. It follows a cumulative approach in contrast to the instrument one, in the sense that the background is integrated over the entire tail length of the coordinate distributions, while the instrument requirements are expressed more as a peak-to-tail ratio. This implies that the cumulative approach presented here leads to an overestimate of the scattering effects by at least half an order of magnitude. For neutron wavelengths above 2.5 Å, the peak-to-tail ratio is higher than 4 orders of magnitude, which means that the current implementation of the MultiBlade detector more than satisfies the ESS reflectometry needs.

Acknowledgments

The authors acknowledge the support from the EU Horizon2020 BrightnESS grant 676548 [51]. This work was supported by the ÚNKP-17-2 new national excellence program of the Hungarian Ministry of Human Capacities. The authors would like to thank ISIS, Didcot, UK and BNC, Budapest, Hungary for the beam time they made available. Computing resources were provided by the DMSC Computing Centre [52]. Gábor Galgóczi would like to thank Balázs Újvári for the fruitful discussions they had.

References

- [1] European Spallation Source ESS ERIC, [Online] Available: <http://europenspallationsource.se/>
- [2] S. Peggs *et al.*, *ESS Technical Design Report*, ESS 2013-001, https://europenspallationsource.se/sites/default/files/downloads/2017/09/TDR_online_ver_all.pdf.
- [3] R. Garoby *et al.*, *The European Spallation Source Design*, *Phys. Scr.* **93** (2018) 014001.
- [4] Fast Reflectometer for Extended Interfacial Analysis - FREIA, [Online] Available: <https://europenspallationsource.se/instruments/freia>
- [5] H. Wacklin, *FREIA: Reflectometer concept for fast kinetics at ESS - instrument proposal* (2016), [Online] Available: https://europenspallationsource.se/sites/default/files/freia_proposal.pdf
- [6] H. Wacklin, *Revealing Change Over Time, FREIA Brings Fast Kinetic Studies to Reflectometry* (2016). [Online] Available: <http://neutronsources.org/news/scientific-highlights/revealing-change-overtime-freia-brings-fast-kinetic-studies-to-reflectometry.html>
- [7] ESTIA, [Online] Available: <https://europenspallationsource.se/instruments/estia>
- [8] J. Stahn, *ESTIA: A truly focusing reflectometer." ESS instrument proposal* (2014), [Online] Available: https://ess-public-legacy.esss.se/sites/default/files/estia_proposal.pdf
- [9] J. Stahn *et al.*, *Focusing specular neutron reflectometry for small samples*, *Eur. Phys. J. Appl. Phys.* **58** (2012) 11001.
- [10] J. Stan *et al.*, *Proposal of the ESTIA instrument* (2014) p.64.
- [11] A. J. Dianoux and G. Lander, *ILL Neutron Data Booklet, Second Edition* (2003).

- [12] D. A. Shea and D. Morgan, *The Helium-3 Shortage: Supply, Demand, and Options Congressional Research Service* (2010).
- [13] R. T. Kouzes, *The ^3He Supply Problem, Technical Report 11-753, US Government Accountability Office* (2011).
- [14] O. Kirstein *et al.*, *Neutron Position Sensitive Detectors for the ESS, PoS (Vertex 2014)* (2014) 029, [Online]. Available: [https://pos.sissa.it/contribution?id=PoS\(Vertex2014\)029](https://pos.sissa.it/contribution?id=PoS(Vertex2014)029)
- [15] I. Stefanescu *et al.*, *A ^{10}B -based neutron detector with stacked MultiWire Proportional Counters and macrostructured cathodes*, *JINST* **8** (2013) P12003.
- [16] J. L. Lacy *et al.*, *The evolution of neutron straw detector applications in homeland security*, *IEEE Trans. Nucl. Sci.* **60** (2013) 1140.
- [17] A. Khaplanov *et al.*, *Multi-Grid Detector for Neutron Spectroscopy: Results Obtained on Time-of-Flight Spectrometer CNCS*, *JINST* **12** (2017) P04030.
- [18] A. Muraro *et al.*, *Performance of the high-efficiency thermal neutron BAND-GEM detector*, *Prog. Theor. Exp. Phys.* **023H01** (2018).
- [19] L. M. S. Margato *et al.*, *Boron-10 lined RPCs for sub-millimeter resolution thermal neutron detectors: conceptual design and performance considerations*, *JINST* **13** (2018) P08007.
- [20] L. M. S. Margato *et al.*, *Boron-10 lined RPCs for sub-millimeter resolution thermal neutron detectors: Feasibility study in a thermal neutron beam*, *arxiv:1809.09677v1* (2018).
- [21] J. Sykora *et al.*, *ZnO:Zn 6 LiF scintillator – low afterglow alternative to ZnS:Ag 6 LiF for thermal neutron detection* Author links open overlay panel, *Nucl. Instrum. Meth.* **A 883** (2018) 75.
- [22] J. Sykora *et al.*, *Large area wavelength shifting fibre thermal neutron detectors using 64 channel flat panel PMTs*, *Conference paper in IEEE NSS MIC conference*, DOI: 10.1109/NSSMIC.2015.7581838 (2015).
- [23] C. L. Wang *et al.*, *Wavelength-Shifting-Fiber Scintillation Detectors for Thermal Neutron Imaging at SNS*, *IEEE Nuclear Science Symposium Conference Record* **He-4-3** (2011).
- [24] S. Jaksch *et al.*, *Recent Developments SoNDe High-Flux Detector Project*, *JPS, Proceedings of International Conference on Neutron Optics (NOP2017)* (2017).
- [25] S. Jaksch *et al.*, *Cumulative Reports of the SoNDe Project*, *arXiv:1707.08679* (2017).
- [26] M. Katagiri, *Neutron detectors with scintillators using ZnS: Ag phosphor: Development summary*, *IEEE NSS, Anaheim* **He-2-2** (2012).
- [27] K. Sakasai *et al.*, *Development of neutron detector for engineering materials diffractometer at J-PARC*, *Nucl. Instrum. Meth.*, **A 600** (2009) 157.
- [28] Z. W. Bell, *Thermal Neutron Detection System Based on ZnS/LiF Scintillator*, *Proceedings of IEEE NSS conference, Anaheim* **He-2-1** (2012).
- [29] S. Lo Meo *et al.*, *Study of silicon+ ^6LiF thermal neutron detectors: Geant4 simulations versus real data*, *Nucl. Instrum. Meth.*, **A 886** (2017) 48.
- [30] A. Mazzone *et al.*, *Geant4 simulations of a novel ^3He -free thermalization neutron detector*, *Nucl. Instrum. Meth.*, **A 889** (2018) 33.
- [31] A. Kok *et al.*, *Silicon sensors with pyramidal structures for neutron imaging*, *JINST* **9** (2014) C04011.
- [32] F. Piscitelli *et al.*, *The Multi-Blade Boron-10-based neutron detector for high intensity neutron reflectometry at ESS*, *JINST* **12** (2017) 03013.

- [33] F. Piscitelli *et al.*, *Characterization of the Multi-Blade 10B-based detector at the CRISP reflectometer at ISIS for neutron reflectometry at ESS*, *JINST* **13** (2018) P05009.
- [34] G. Mauri, F. Messi *et al.*, *Fast neutron sensitivity of neutron detectors based on boron-10 converter layers*, *JINST* **13** (2018) P03004.
- [35] F. Piscitelli, *Boron-10 layers, neutron reflectometry and thermal neutron gaseous detectors*, *Doctoral thesis, University of Perugia/ILL* (2014), *arXiv:1406.3133*.
- [36] G. Mauri *et al.*, *Neutron reflectometry with the Multi-Blade ¹⁰B-based detector*, *Proc. R. Soc. A* **474**, 20180266 (2018).
- [37] F. Piscitelli and P. Van Esch, *Analytical modeling of thin film neutron converters and its application to thermal neutron gas detectors*, *JINST* **8** (2013) P04020.
- [38] S. Agostinelli *et al.*, *Geant4 - A Simulation Toolkit*, *Nucl. Instrum. Meth. A* **506** (2003) 250.
- [39] J. Allison *et al.*, *Geant4 developments and applications*, *IEEE Trans. Nucl. Sci.* **53** (2006) 07.
- [40] J. Allison *et al.*, *Recent Developments in Geant4*, *Nucl. Instrum. Meth. A* **835** (2016) 186.
- [41] Institute Laue-Langevin, [Online] Available: <http://www.ill.eu>
- [42] J. C. Buffet *et al.*, *Advances in detector for single crystal neutron diffraction*, *Nucl. Instrum. Meth. A* **554** (2005) 392.
- [43] F. Sauli, *Principles of operation of multiwire proportional and drift chambers*, *Lectures given in the Academic Training Programme of CERN* (1977).
- [44] F. Piscitelli *et al.*, “Neutron reflectometry on highly absorbing films and its application to 10B4C-based neutron detectors,” *Proc. R. Soc. A*, vol. 472, p. 03013, 2016.
- [45] T. Kittelmann *et al.*, *Geant4 Based Simulations for Novel Neutron Detector Development*, *J. Phys. Conf. Ser.* **513** (2014) 022017.
- [46] K. Kanaki *et al.*, *Simulation tools for detector and instrument design*, *Physica B*, Proceedings of the ICNS conference, <https://doi.org/10.1016/j.physb.2018.03.025> (2017).
- [47] X.X. Cai and T. Kittelmann, *NCrystal: a library for thermal neutron transport in crystals*, [Online] Available: <https://doi.org/10.5281/zenodo.853186>, <https://mctools.github.io/ncrystal/>
- [48] E. Dian *et al.*, *Scattered neutron background in thermal neutron detectors*, *Nucl. Instrum. Meth. A* **902** (2018) 173.
- [49] A. Carmona Basañez *et al.*, *DECAL, a Python tool for the efficiency calculation of thermal neutron detectors based on thin-film converters*, *arXiv:1801.07124* (2018).
- [50] ISIS Neutron and Muon Source, [Online] Available: <https://www.isis.stfc.ac.uk/Pages/home.aspx>
- [51] BrightnESS, [Online] Available: <https://brightness.esss.se/>
- [52] Data Management & Software Centre, [Online] Available: <https://europanspallationsource.se/data-management-software/computing-centre>
- [53] K. Lefmann and K. Nielsen, *McStas, a general software package for neutron ray-tracing simulations*, *Neutron News* **10** (1999) 20.
- [54] P. Willendrup, E. Farhi, and K. Lefmann, *McStas 1.7 - a new version of the flexible Monte Carlo neutron scattering package*, *Physica B* **350** (2004) E735.
- [55] ANTS2: a simulation and experimental data processing package for Anger camera-type detectors, [Online] Available: <http://coimbra.lip.pt/ants/ants2.html>

[56] NCrystal data library, [Online] Available: <https://github.com/mctools/ncrystal/wiki/Data-library>

A NCrystal cross sections

For the correct treatment of the interaction of thermal and cold neutrons with several single crystals, poly-crystalline materials and powders, the NCrystal library [46, 47] is used in this work. The treatment includes both coherent elastic (Bragg) diffraction and various models for the inelastic scattering. The library is publicly available for use under a highly liberal open source license (Apache 2.0) and already interfaces with several Monte Carlo packages, e.g. McStas [53, 54], ANTS2 [55] and Geant4. Its flexible interface though allows for easy integration with other packages.

Two application examples that are used in this work are Ti and Al, presented in figure 10. The reproduction of the respective scattering cross sections would not be possible without NCrystal. The library has been validated against available experimental data. A collection of existing crystalline structures supported by NCrystal can be found in [56].

A visual demonstration of the various types of scattering in the detector blade and window appears in figure 11a. Coherent elastic scattering takes place when the neutron wavelength is below the Bragg cut-off value of the materials it is transported in (4.67 Å for Al and 5.14 Å for Ti). What the figure presents for a neutron wavelength of 2.5 Å is the difference between the polar angle of a neutron at its conversion point - calculated from its momentum vectors - and the initial polar angle with which it is generated:

$$\delta\Theta = \Theta_{conversion} - \Theta_{initial}. \quad (\text{A.1})$$

The red distribution contains only the contributions from gas and converter, as the blade and window materials are set to vacuum. No Bragg scattering takes place with these conditions, as the remaining materials are not crystalline. Once the blade material is set to Ti, structures from the Debye-Scherrer

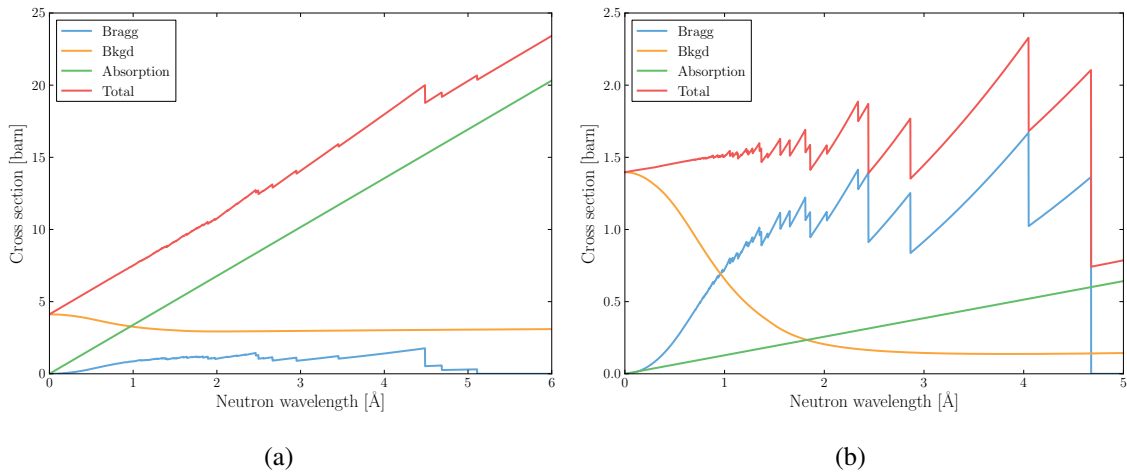


Figure 10: (a) Total scattering and absorption cross sections of Ti and (b) Al vs. neutron wavelength. “Bkgd” refers to coherent inelastic, elastic incoherent and inelastic incoherent processes.

cones become apparent (in green). Similarly, the Bragg scattering from the Al window appears in the remaining two distributions (yellow, blue).

By selecting “background” neutrons, as defined in the denominator of equation 3.1, and switching off Bragg scattering in the simulation, it is estimated that about 30% of the neutrons scatter coherently elastically for 2.5 Å and a 2 mm Al window (see figure 11b).

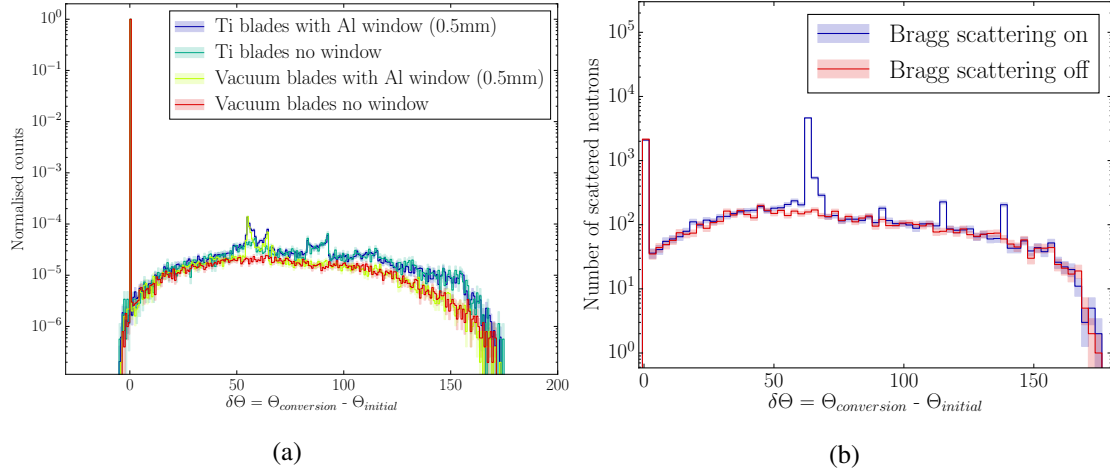


Figure 11: (a) Difference between the conversion polar angle and the primary polar angle for neutrons for a neutron wavelength of 2.5 Å. Coherent elastic scattering on the Al detector window and the Ti blades is responsible for the structures appearing around 50°, 80° and 150°. (b) Same distribution for “background” neutrons only and with both Al and Ti present. The red distribution disables Bragg scattering in the detector materials.